Research Article Vol. 14, No. 3 / March 2026 / Photonics Research 731

PHOTONICS Research

Silicon photonic integrated carrier-extracted self-coherent receiver

Haojie Zhu,[1] Yuhao Fang,[1] Jiwei Xie,[1] Weiqi Lu,[1] Zhen Wang,[2] Dayu Shi,[1] Puzhen Yuan,[1] Honglin Ji,[3] Lan Li,[1,4] Yikai Su,[5] and William Shieh[1,4,*]

[1]School of Engineering, Westlake University, Hangzhou 310030, China
[2]The Aerospace Laser Technology and Systems Department, Shanghai Institute of Optics and Fine Mechanics, Chinese Academy of Sciences, Shanghai 201800, China
[3]Peng Cheng Laboratory, Shenzhen 518055, China
[4]Westlake Institute for Optoelectronics, Hangzhou 311421, China
[5]Department of Electronic Engineering, Shanghai Jiao Tong University, Shanghai 200240, China
*Corresponding author: shiehw@westlake.edu.cn

Received 12 August 2025; revised 27 October 2025; accepted 23 November 2025; posted 26 November 2025 (Doc. ID 575995); published 26 February 2026

To overcome the fiber chromatic dispersion (CD)-induced power fading in intensity modulation direct detection (IM/DD), self-coherent detection is an advanced DD solution enabling optical field recovery without local oscillators (LOs) for CD compensation. For cost-efficient and high-performance short-reach links, we propose carrier-extracted self-coherent (CESC) detection, which derives the LO from the incoming signal by employing a narrowband coupled-resonator optical waveguide (CROW) filter. Thus, the signal-to-signal beat interference (SSBI) could be effectively suppressed, enabling complex-valued double-sideband signal retrieval with linear equalization only. In this work, we demonstrate, to our knowledge, the first silicon photonic integrated CESC receiver, achieving 303.8-Gb/s data rate over 50-km standard single-mode fiber using a 62-Gbaud PCS-64QAM signal at a low carrier-to-signal power ratio (CSPR) of 0 dB with only linear equalizers, which is promising for short-reach links in datacenters and access networks.

https://doi.org/10.1364/PRJ.575995

1. INTRODUCTION

The exponential proliferation of artificial intelligence (AI) and machine learning workloads—particularly large-scale model training and real-time inference—has triggered unprecedented bandwidth demands in datacenter interconnects [1,2]. These applications impose stringent requirements for ultra-low-latency, high-throughput communication, driving short-reach optical networks toward terabit-scale capacity while confronting critical power, size, and cost efficiency constraints [3–5]. With a simple structure and low-cost advantage, conventional intensity modulation direct detection (IM/DD) is always the primary candidate for short-distance communications [6,7]. However, facing an ever-increasing capacity demand, IM/DD systems are hard to overcome fundamental limitations in dispersion tolerance and spectral efficiency [6,8]. Beating with a strong local oscillator (LO), coherent detection can easily realize optical field retrieval with a high sensitivity [9]. With the capability of conveying complex-valued double-sideband (DSB) signals, the spectral efficiency of coherent detection is also very superior to the IM/DD counterpart. While coherent detection offers high performance, its deployment in cost-sensitive short-reach applications (<80 km) remains hampered by expensive narrow-linewidth lasers and power-hungry digital signal processing (DSP) [10]. To bridge this gap, self-coherent detection has been proposed to retrieve complex-valued DSB signals without LOs. As an advanced direct detection, self-coherent detection could be a cost-effective and energy-efficient scheme for the short-distance networks [11–14].

To further reduce the cost and power consumption of the transceivers implemented in the short-reach communications, which is cost- and energy-sensitive, integration technology becomes a critical solution [15,16]. Silicon photonics emerges as a transformative platform, enabling monolithic integration of photonic and electronic components to address scalability, footprint, and cost challenges [17,18]. Under this paradigm, self-coherent detection represents a promising compromise, delivering coherent-like full-field signal recovery without LOs by leveraging a transmitted optical carrier along with the signal [12,13]. Recent SiP-based prototypes [19,20] of self-coherent detections, including Stokes vector direct detection (SVDD) and carrier-assisted differential detection (CADD), validate the viability of this approach, providing a promising solution for short-reach networks. Since SVDD faces scalability challenges to four-dimensional transmission and

CADD suffers from signal-to-signal beat interference (SSBI) impairment requiring computationally intensive cancellation algorithms, there exists a critical need for more practical and simplified self-coherent architectures. The carrier-extracted self-coherent (CESC) detection scheme addresses this challenge by deploying a narrowband filter to extract a purified carrier from the transmitted self-coherent signal, enabling coherent-like detection performance without LOs [21]. Crucially, filter-enabled suppression of signal components permits signal recovery via linear equalization along with effective elimination of SSBI. Inherently compatible with coherent DSP and receiver architectures, CESC detection positions itself as a promising solution for next-generation short-reach interconnects.

In this work, we propose and experimentally validate a CESC receiver integrated on a SiP platform. The integrated CESC receiver achieves a 303.8-Gb/s transmission data rate over 50-km standard single-mode fiber (SSMF) using 62-Gbaud probabilistic constellation-shaped 64QAM (PCS-64QAM) with 4.9-bits/symbol entropy. The proposed architecture employs an optimized second-order coupled resonator optical waveguide (CROW) filter to achieve high-purity carrier extraction, enabling low 0-dB carrier-to-signal power ratio (CSPR) and a 3-GHz guard band. With effective suppression of signal components provided by the CROW filter, only linear equalization is needed to recover the transmitted signal, eliminating complex SSBI cancellation algorithms. Featuring LO-free and coherent-like architectures, the CESC receiver could be a pivotal solution for cost-effective and high-performance short-reach interconnects.

2. PRINCIPLE AND FABRICATION

A. Carrier-Extracted Self-Coherent Detection Principles

To recover the optical field, an optical carrier is necessary for beating with the transmitted signal to produce the linear signal-carrier beating term. We denote the carrier and signal fields as C and S, respectively. Assuming a photodetector responsivity of unity for simplicity, the photocurrent I generated via square-law detection is given by

$$I = |S + C|^2 = |S|^2 + |C|^2 + \mathrm{Re}(S \cdot C^*). \quad (1)$$

The operator Re(·) takes the real component of a complex value, while '*' represents complex conjugation. In Eq. (1), the third term represents the essential linear beating term for signal recovery. Conventional IM/DD systems inherently operate on real-valued signals, confining information transmission to a single dimension. This architecture fundamentally precludes the recovery of complex-valued DSB signals due to the absence of quadrature (imaginary) components. Consequently, coherent detection emerges as a critical advancement, enabling full complex-field reconstruction of DSB signals and thereby achieving superior spectral efficiency.

Figure 1(a) presents the coherent detection scheme. While a strong carrier beats with the received signal, the optical outputs from the optical hybrid are captured by two BPDs. The photocurrents I_1 and I_2 produced by BPDs can be represented as

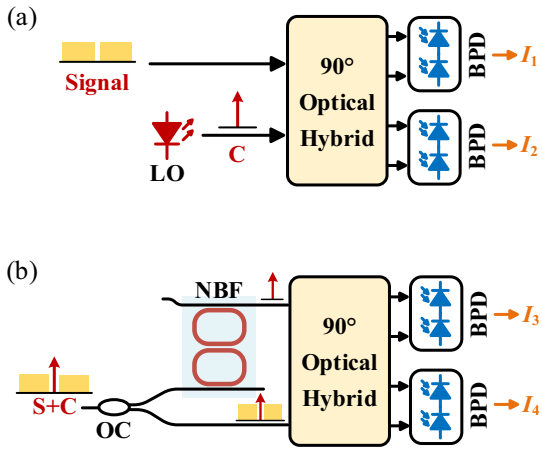

Fig. 1. Schematics of (a) conventional coherent detection and (b) carrier-extracted self-coherent detection. C: carrier. S: signal. NBF: narrow-bandwidth filter. BPD: balanced photodetector.

$$I_1 = |S + C|^2 - |S - C|^2 = 4\,\mathrm{Re}(S \cdot C^*), I_2 = |S + j \cdot C|^2 - |S - j \cdot C|^2 = 4\,\mathrm{Im}(S \cdot C^*), \quad (2)$$

where j denotes the imaginary unit and Im(·) represents the imaginary component. Consequently, Eq. (2) enables reconstruction of the complex-valued transmitted signal through simultaneous recovery of its in-phase and quadrature components, achieving full-field recovery. This principle extends to self-coherent detection, where a co-transmitted optical carrier facilitates signal field reconstruction. Beating with this co-transmitted carrier, the essential linear beating terms for both real and imaginary signal components are generated. In the proposed CESC architecture as presented in Fig. 1(b), the received composite signal is split into dual paths: one branch is fed directly into a 90° optical hybrid, and the other branch employs a narrow-bandwidth filter to extract a purified carrier. Subsequently, self-coherent beating between the transmitted signal and extracted carrier enables complex-field reconstruction analogous to the conventional coherent detection. The resulted photocurrents I_3 and I_4 are given by

$$I_3 = 4\,\mathrm{Re}[(S + C) \cdot C^*] = 4\,\mathrm{Re}(S \cdot C^* + C \cdot C^*), \quad I_4 = 4\,\mathrm{Im}[(S + C) \cdot C^*] = 4\,\mathrm{Im}(S \cdot C^* + C \cdot C^*). \quad (3)$$

In Eq. (3), we can easily get the signal-carrier beating terms with a carrier-carrier beating term $C \cdot C^*$. While $C \cdot C^*$ constitutes a non-informative direct current bias in the electrical domain, it is readily eliminated during DSP via direct current blocking. Consequently, the CESC detection can be treated as a coherent detection in principle. Processing the optical signal detected by the two BPDs can well recover the transmitted complex-valued DSB signal without separate LOs, compatible with standard coherent DSP. When extending to dual-polarization systems, an adaptive polarization controller (APC) could be used to ensure the presence of a robust optical carrier for each polarization state [22,23].

Notably, the expressions of photocurrents I_3 and I_4 presented by Eq. (3) are obtained under an ideal condition that

the extracted carrier is entirely pure and all signal components have been totally rejected. Consequently, there is no signal-to-signal beat interference (SSBI) produced in this ideal situation. However, signal components may not be well suppressed in the actual scenarios if the filter cannot provide a narrow bandwidth and a high extinction ratio (ER) for carrier extraction. After filtering, the residual signal components will produce a non-negligible SSBI, affecting the system performance. Therefore, a filter with a narrower bandwidth and a higher ER is preferred in the CESC detection systems since it can significantly reduce the residual signal components and greatly alleviate the SSBI influence on the CESC systems. Thereby, the transmitted signal can be retrieved without a complex SSBI cancellation algorithm.

In summary, by deploying a filter with a narrow bandwidth and a high ER for carrier extraction to ensure the purity of the extracted carrier, the complex-valued DSB signal can be recovered under linear equalization with greatly mitigated SSBI.

B. Silicon Photonic CESC Receiver Chip

The 3D schematic diagram and microscope image of the SiP CESC detection chip are plotted in Figs. 2(a) and 2(b). The devices employed in the CESC receiver were fabricated on the 220-nm-thick silicon-on-isolator (SOI) platform based on the standard complementary metal oxide semiconductor (CMOS) manufacturing process. The overall footprint of the monolithic CESC receiver chip is approximately 1.8 mm × 0.89 mm, which is calculated by rectangular approximation of its area. The received optical signal is coupled to the chip by a grating coupler (GC), subsequently passing through a tunable coupler to yield a dual-branch optical signal with an optimized power splitting ratio, compensating for the insertion loss of the CROW filter. The optimized power splitting ratio is to maximize the waveforms of the output photocurrent. The tunable coupler is constructed by a 1 × 2 MMI, two thermo-optic phase shifters (TOPSs), and a 2 × 2 MMI. Applying a voltage bias on the TOPSs, the phase difference between the two arms follows the changes; thereby, the two output powers of the 2 × 2 MMI will also be tuned according to the power-splitting ratio. After an optimal power division via the tunable coupler, one branch goes through the CROW filter, characterized by a narrow bandwidth that selectively permits the optical carrier to traverse while suppressing the signal components. There is an optical power monitor (OPM) and a GC

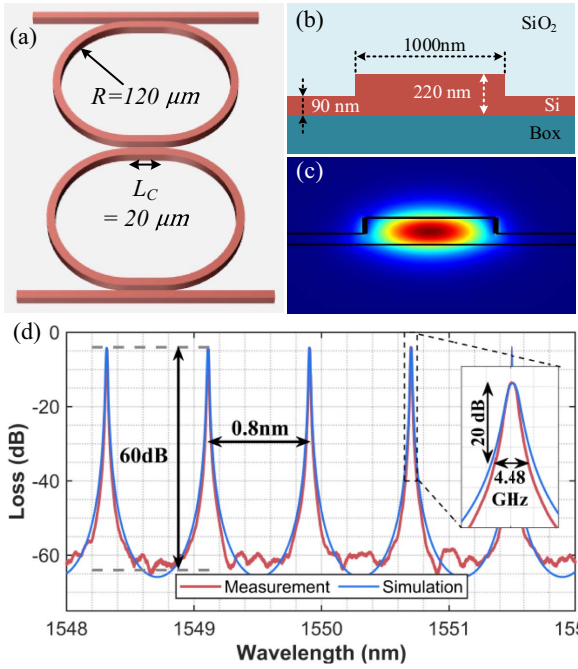

Fig. 3. (a) Symmetric CROW filter structure. (b) Cross section and (c) fundamental mode of the CROW filter's waveguide. (d) Transmission spectra of our designed and fabricated CROW filter with a 0.1-pm resolution (the loss has been normalized by removing the on- and off-chip coupling losses). R: radius. L_C: coupling length.

connected to the filter drop port by two 1:19 power-splitting-ratio DCs. The other branch is first split into two paths with equal power via a 1 × 2 MMI. One passes directly to the optical hybrid to beat with the filtered optical carrier, and the other goes to an OPM for signal power monitoring. The resulting four optical outputs are detected by two BPDs for signal retrieval. Notably, all the OPMs are used to monitor the power of signal components and the filtered carrier if needed, rather than the signal recovery.

The two on-chip BPDs consist of four germanium PDs with a responsivity of 0.96 A/W, and the optical hybrid function is realized by a 2 × 4 MMI, which exhibits an excess loss of 2.8 dB. Significantly, the narrowband CROW filter employs a 1-μm-wide ridge waveguide to alleviate the sidewall scattering [24,25] as depicted in Figs. 3(a)–3(c). To achieve a narrow

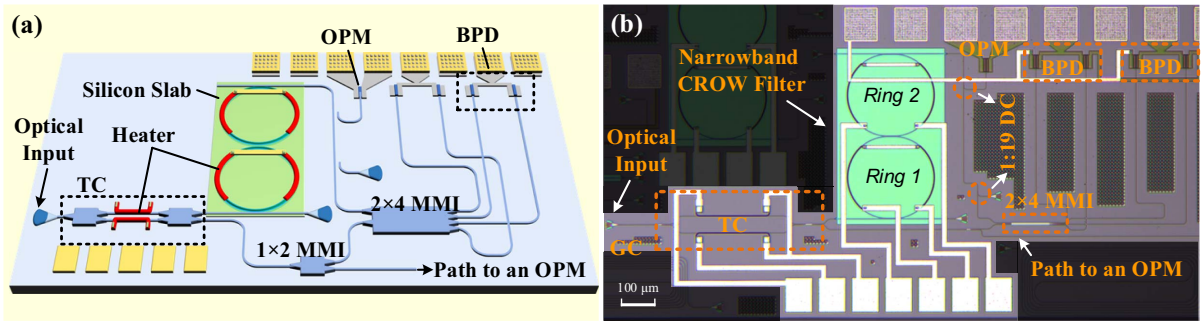

Fig. 2. (a) 3D diagram of CESC detection chip design. (b) Micrograph of SiP CESC detection chip. GC: grating coupler. MMI: multi-mode interference. DC: directional coupler. TC: tunable coupler. OPM: optical power monitor.

bandwidth and a high extinction ratio, a symmetric second-order micro-ring cascaded scheme with a big radius and small coupling coefficients is deployed in the filter design [26,27]. Figure 3(d) shows the filter exhibits a 4.48-GHz 20-dB bandwidth, a 4-dB insertion loss, and a ~60-dB extinction ratio (ER), which can provide an effective rejection of signal components. The measured transmission spectra of the manufactured CROW filter also demonstrate a good consistency with the design. In the experiment, a 5-V bias voltage is applied to the BPDs, and the electrical radio frequency (RF) signals produced by the BPDs are detected by a multi-channel RF probe. The contact pads are arrayed with a period of 150 μm.

3. EXPERIMENTAL SETUP

Figure 4 illustrates the experimental setup for measuring the SiP CESC detection system. Within this setup, the light emitting from a Santec (TSL-570) external cavity laser (ECL) at a wavelength of 1550.4 nm is split into two distinct branches. One branch serves as the optical carrier, while the other is designated for signal generation through an IQ modulator driven by a Keysight (M8194A) arbitrary waveform generator (AWG) sampling at 120 GSa/s. To ensure the optical signal and carrier are transmitted in one polarization, a polarizer is employed on the transmitter side, and the polarizations of the two branches are adjusted to align the polarizer by two polarization controllers (PCs). Subsequently, the modulated signal is recombined with the optical carrier to form a self-coherent signal to transmit after boost amplification by EDFA. At the receiver end, the received signal is first pre-amplified and then coupled into the SiP CESC receiver chip via the grating coupler. The PC deployed after the EDFA is used to set the polarization of the received optical signal to align with the on-chip grating coupler for efficient coupling. This receiver chip produces two RF outputs, acquired by an 80-GSa/s Keysight (DSAV334A) real-time oscilloscope (RTO) for offline DSP.

In the experiment, a variable optical attenuator (VOA) is implemented in the optical carrier arm at the transmitter end to adjust the carrier-to-signal power ratio (CSPR). Furthermore, the VOA adopted at the receiver end before EDFA pre-amplification is used to adjust the received optical power (ROP) to characterize the CESC receiver's sensitivity. The modulation scheme adopted in this experiment combines orthogonal frequency division multiplexing (OFDM) with PCS-64QAM, and a 3-GHz guard band is introduced in the middle of the OFDM signal for carrier extraction. In the experiment, two signals are transmitted: (1) a 50-Gbaud PCS-64QAM (entropy = 4.8 bits/symbol) signal corresponding to a 240-Gb/s data rate, and (2) a 62-Gbaud PCS-64QAM (entropy = 4.9 bits/symbol) signal corresponding to a 303.8-Gb/s data rate.

The utilized DSP algorithms are shown in Fig. 4. After PCS-QAM mapping and OFDM modulation with a discrete Fourier transform (DFT) size of 2048, frequency domain pre-emphasis is employed to enhance bandwidth performance. To prevent a high peak-to-average power ratio (PAPR) introducing a non-negligible DAC quantization noise, PAPR clipping is implemented to avoid system performance degradation [19]. In the receiver-side DSP, the signal is first resampled to

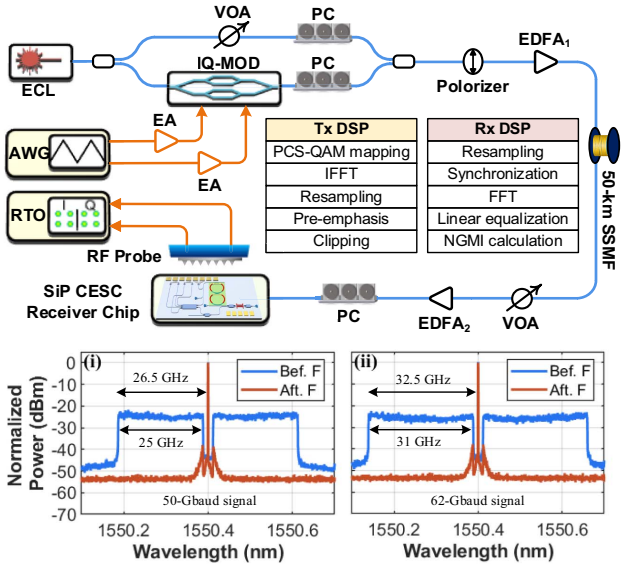

Fig. 4. Experimental setup for measuring our designed SiP CESC receiver chip. Insets: (i), (ii) optical spectra of received signal before and after filtering with a 1.12-pm resolution at 50 and 62 Gbaud, respectively. Bef. F: before filtering. Aft. F: after filtering. ECL: external cavity laser. IQ-MOD: IQ modulator. EA: electrical amplifier. AWG: arbitrary waveform generator. VOA: variable optical attenuator. PC: polarization controller. EDFA: erbium-doped fiber amplifier. RTO: real-time oscilloscope.

ensure its sampling rate is equal to the transmitted data. After synchronization, linear equalization is deployed to compensate for the signal impairments during the transmission to retrieve the transmitted signal. Finally, the normalized generalized mutual information (NGMI) is calculated to characterize the performance of the fabricated CESC receiver.

4. RESULTS AND DISCUSSION

Within self-coherent detection systems, the CSPR constitutes a critical optimization parameter governing system performance. A fundamental trade-off exists between the linear beating term magnitude and the effective signal power dominated by the CSPR selection. Elevated CSPR values enhance carrier power to beat with the transmitted signal but concomitantly suppress data-bearing signal power, degrading the receiver performance. Theoretically, a CSPR of 0 dB maximizes desired carrier-signal beating terms for recovering the transmitted signal while preserving signal integrity in the conventional self-coherent detection systems, representing the theoretical optimum.

Figure 5 quantifies CSPR optimization for the proposed CESC receiver under optical back-to-back (OBTB) and 50-km SSMF transmission scenarios at 50 Gbaud and 62 Gbaud. Optimal performance consistently occurs at 0-dB CSPR across all configurations—a significant achievement enabled by the well-engineered CROW filter. This CROW filter critically suppresses signal components within the carrier extraction, as evidenced by high-resolution (1.12-pm) optical spectra of received signals before and after filtering plotted in Fig. 4 insets (i) and (ii).

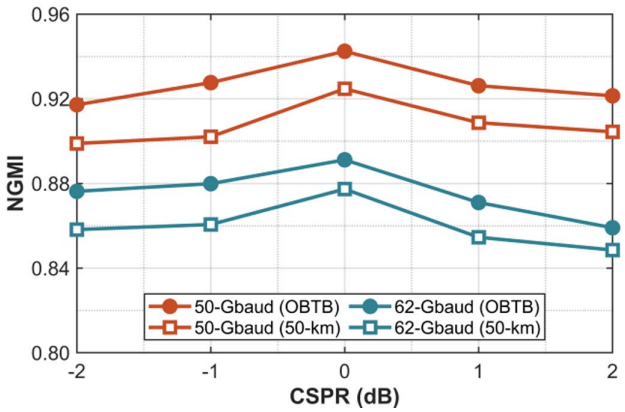

Fig. 5. NGMI performance versus CSPR in both OBTB and 50-km SSMF transmission cases with varied signal baud rates (50 Gbaud and 62 Gbaud). NGMI: normalized generalized mutual information.

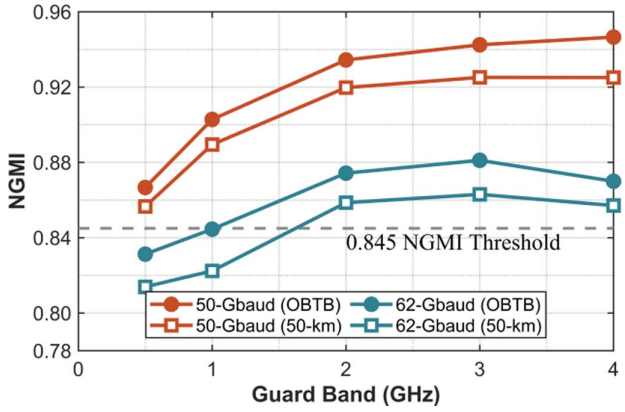

Fig. 6. NGMI performance versus signal guard band in both OBTB and 50-km SSMF transmission cases with varied signal baud rates (50 Gbaud and 62 Gbaud).

The significant signal suppression performance permits low CSPR operation while substantially mitigating SSBI penalties without complex SSBI cancellation algorithms. Conversely, inadequate filter suppression necessitates higher CSPR to alleviate residual-signal-induced SSBI degradation. However, high CSPR operation introduces dual penalties: (1) reduced effective signal power, and (2) exacerbated fiber nonlinear impairments including stimulated Brillouin scattering (SBS) [28] and Kerr effects [29] at elevated launch powers, ultimately degrading system performance. The CESC receiver's low-CSPR capability based on a second-order CROW filter thus enables higher launch power tolerance, extending system power margins. Consequently, achieving SSBI-resilient operation at low CSPR necessitates filters with narrow bandwidths and high extinction ratios—which is imperative for CESC receivers.

Figure 6 presents the signal guard band optimization results in the OBTB and 50-km SSMF transmission cases with 50-Gbaud and 62-Gbaud signals, respectively. When the signal guard band is greater than or equal to 2 GHz, the NGMI performance is greatly improved compared with 0.5-GHz and 1-GHz signal guard bands, demonstrating that the SSBI penalties have been greatly alleviated with suppressed residual signal components. In theory, a wider guard band leads to better system performance. However, when the guard band equals 4 GHz in the 62-Gbaud signal transmission cases, the received signal approaches the cut-off frequency of RTO, causing a slight NGMI performance degradation. Considering a trade-off between electrical spectral efficiency (ESE) and CESC system performance introduced by the signal guard bandwidth, a 3-GHz guard band is deployed in this experiment. Notably, employing a carrier-extraction filter with a narrower bandwidth and a higher extinction ratio can further reduce the signal guard band to enhance ESE. This is also the most important future optimization direction for the CESC receiver. Furthermore, iterative algorithms or nonlinear equalizations could be employed to improve signal recovery with a 0.5-GHz guard band, potentially enhancing ESE compared to the 3-GHz case. Nevertheless, the associated increase in DSP complexity and power consumption renders these marginal improvements impractical, especially as the signal baud rate increases.

As illustrated in Fig. 7(a), the launch power of the CESC system in 50-km SSMF transmission cases has been optimized. Elevating the transmitter-end EDFA amplifying power to enhance launch power will introduce a big amplified spontaneous emission (ASE) noise, which is the major source of noise in the optical-fiber channels, degrading the system performance. Besides, high launch power may also intensify the fiber nonlinearity effects [28,29], such as SBS. Moreover, extending the transmission fiber length will also reduce the launch power tolerance. Taking these effects into consideration, the optimization results reflect that when launch power $\leq$10 dBm, the NGMI performance differences are very small. Thereby, if a large power margin is a more important parameter for the communication, we can properly increase the launch power. In this experiment, to characterize the best receiver sensitivity, 9-dBm launch power is optimum.

Under 9-dBm launch power, 0-dB CSPR, and 3-GHz signal guard band, we characterize the CESC receiver's sensitivity by the NGMI as a function of ROP for four scenarios, as depicted in Fig. 7(b). With a 240-Gb/s data rate, the SiP CESC receiver demonstrates an ROP sensitivity of approximately −27.5 dBm in the OBTB scenario and around −26 dBm in the 50-km SSMF transmission scenario, considering a 0.845 NGMI threshold [30]. While the data rate is 303.8 Gb/s, the ROP sensitivities are approximately −20.5 dBm and −18.5 dBm in OBTB and 50-km SSMF transmission cases, respectively. In addition, we employ a grating coupler for the CESC receiver chip's optical input in this experiment, which incurs an approximately 5.5-dB on-chip coupling loss in the 1550-nm wavelength region. Hence, if a low-coupling-loss edge coupler and a lens fiber are implemented in this chip design and measurement, the on-chip coupling loss can be greatly reduced, further enhancing the integrated CESC receiver's sensitivity. The insets (i)–(iv) provide the retrieved constellations of 50-Gbaud and 62-Gbaud PCS-64QAM signals in the two transmission cases, respectively. The results show a great receiver sensitivity, well verifying the SiP CESC receiver's performance.

To characterize the on-chip CESC receiver's maximum transmission capacity in this experimental setup, we adopt varying entropies of transmitted 50-Gbaud and 62-Gbaud

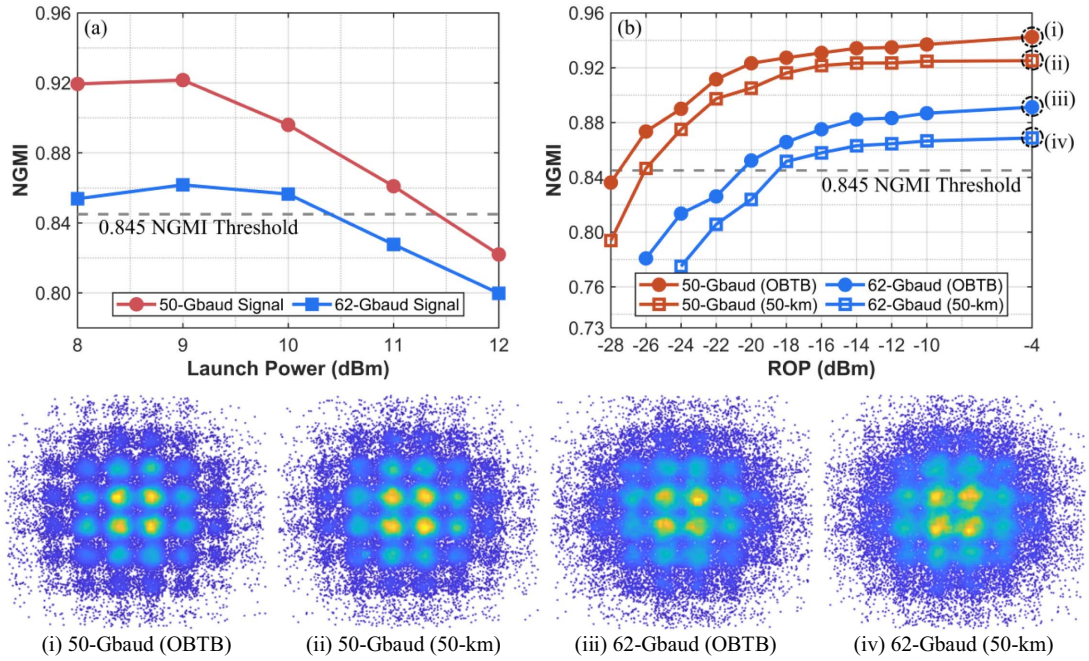

Fig. 7. (a) NGMI performance versus launch power in 50-km SSMF transmission case with 50-Gbaud and 62-Gbaud signals; (b) NGMI versus ROP in both OBTB and 50-km SSMF transmission cases with varied signal baud rates (50 Gbaud and 62 Gbaud). Insets: recovered constellations of four cases.

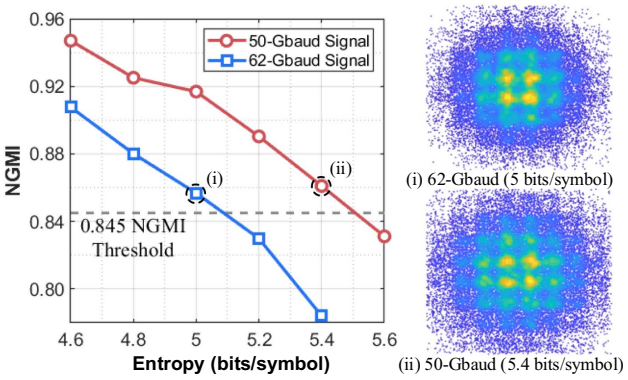

Fig. 8. NGMI performance versus loaded entropy of the PCS-64QAM signal with 50-Gbaud and 62-Gbaud baud rates in 50-km SSMF transmission. Insets: recovered constellations of (i) 62-Gbaud PCS-64QAM signal with an entropy of 5 bits/symbol and (ii) 50-Gbaud PCS-64QAM signal with an entropy of 5.4 bits/symbol.

PCS-64QAM signals in the 50-km SSMF transmission cases as depicted in Fig. 8. Under a 0.845 NGMI threshold [30], 50-Gbaud signal can achieve a maximum entropy of around 5.4 bits/symbol corresponding to 270-Gb/s data rate, and 62-Gbaund signal enables a 310-Gb/s transmission data rate with a maximum entropy of 5 bits/symbol. Future transmission capacity improvement of this CESC receiver chip in this experiment can be realized by leveraging high-bandwidth components including the modulator and the entropy loading technique for each subcarrier [31,32].

5. CONCLUSION

In this paper, we have demonstrated 303.8-Gb/s PCS-64QAM signal transmission over 50-km SSMF by an integrated SiP CESC receiver based on a second-order CROW filter. Providing a good rejection of signal components by the CROW filter because of its narrow bandwidth and high ER, the SSBI penalty has been significantly mitigated with a low CSPR of 0 dB. Hence, only linear equalization is needed to recover the transmitted signal, compatible with coherent DSP. Based on the excellent transmission performance and cost-efficient scheme, the CESC detection could play a significant role in high-capacity short-reach interconnects in the future.

APPENDIX A: NARROWBAND FILTER AND TUNABLE COUPLER DESIGN

In integrated receiver applications, the insertion loss (IL) of coupled resonator optical waveguide (CROW) filters represents a critical performance metric. Consequently, the minimization of waveguide propagation losses constitutes an essential design consideration. Among various loss mechanisms, sidewall scattering is widely recognized as the dominant contributor to overall propagation losses. The Payne–Lacey (PL) model [33] has established the standard analytical framework for quantifying this phenomenon, providing a closed-form solution that characterizes scattering losses in two-dimensional waveguide structures. The scattering loss coefficient α (dB/unit length) is expressed as

$$\alpha = 4.34 \frac{\sigma^2}{\sqrt{2} k_0 d^4 n_1} g \cdot f, \tag{A1}$$

where σ denotes the root-mean-square roughness, k_0 is the free-space wavenumber, d is the waveguide half-width, and n_1 represents the waveguide-core refractive index. The function g depends exclusively on waveguide geometry, while f is governed by the correlation length and refractive index contrast. Eqution (A1) demonstrates that waveguide width expansion effectively mitigates scattering losses. Ridge waveguides exhibit reduced scattering losses compared to strip waveguides due to their diminished sidewall surface area [25]. Correspondingly, we implement 1-μm-wide ridge waveguides in the CROW filter design.

Under symmetric design conditions, the coupling coefficient between each bus waveguide and ring waveguide is k_1, while the inter-ring coupling coefficient is k_2. By modeling each coupling region as a lumped junction, the electric field expression for the drop port is derived as follows:

$$E_{\text{drop}} = \frac{-j\alpha_r k_1^2 k_2 \exp(j\cdot\theta)}{1 - 2\alpha_r t_1 t_2 \exp(j\cdot\theta) + \alpha_r^2 t_1^2 (k_2^2 + t_2^2)\exp(j\cdot 2\theta)}, \tag{A2}$$

where j, α_r, θ, t_1, and t_2 are the imaginary unit, round-trip transmission factor, round-trip phase delay of a ring, bus-ring-waveguide transmission coefficient, and inter-ring-waveguide transmission coefficient, respectively. In the lossless coupling condition, the relationship between coupling coefficients and transmission coefficients satisfies $k_i^2 + t_i^2 = 1$ $(i = 1, 2)$. To achieve a narrow bandwidth while maintaining low insertion loss, the coupling coefficients are optimized under a minimal IL condition for the drop port [26]. Via 3D finite-difference time-domain (FDTD) solutions, the bus-ring-waveguide and inter-ring-waveguide gaps can be determined as 276 nm and 521 nm, respectively.

As a multi-mode waveguide (MWG), the 1-μm-wide ridge waveguide supports TE_0, TE_1, and TE_2 modes. Consequently, fundamental-mode propagation within the ring cavity must be verified through simulation [34]. As illustrated in Fig. 9, the mode excitation ratios (MERs) for both TE_1 and TE_2 modes demonstrate efficient adiabatic characteristics in the MWG at a radius of 120 μm. To further optimize the adiabatic characteristics of the MWG bends, the adoption of Euler bends is a promising approach [34]. When light couples into the carrier-extracted self-coherent (CESC) receiver chip via a grating coupler, it initially propagates through a 0.5-μm-wide strip waveguide. Waveguide transition tapers are therefore implemented to convert the 0.5-μm-wide strip waveguide to the 1-μm-wide ridge waveguide required for the CROW filter. The transition structure (Fig. 10) features an initial taper to a 0.5-μm-wide ridge waveguide, followed by a subsequent taper expanding the waveguide width to 1 μm.

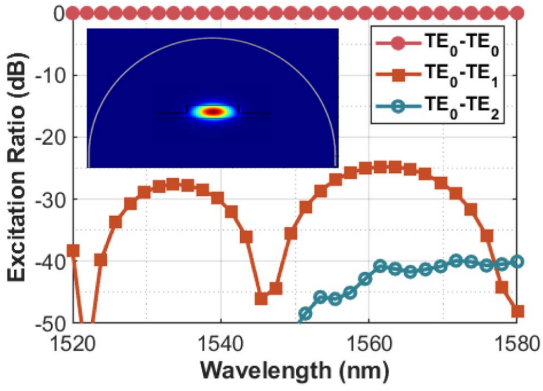

Fig. 9. Calculated light transmissions in the waveguide consisting of an input straight MWG, a 180° circular MWG, and an output straight MWG. MWG: multi-mode waveguide.

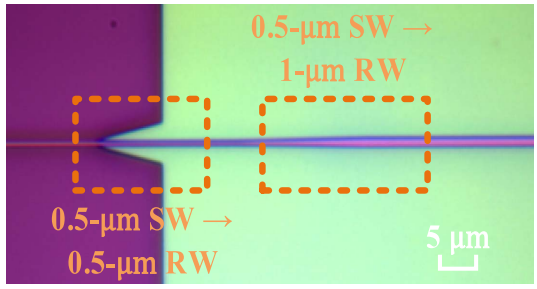

Fig. 10. Microscope image of the waveguide transition tapers. SW: strip waveguide. RW: ridge waveguide.

The tunable coupler serves to adjust the power-splitting ratio for mitigating the IL of the narrowband CROW filter, thereby optimizing the transmission performance of the CESC receiver chip. Figure 11(a) illustrates the 3D schematic of the tunable coupler, which employs a Mach–Zehnder interferometer (MZI) structure comprising a 1 × 2 multi-mode interference (MMI) coupler, thermo-optic phase shifters (TOPSs), and a 2 × 2 MMI coupler. The transfer matrix of this device can be analytically derived [35,36] as shown in Fig. 11. Similar to the on-chip MZI-based optical switches [37,38], the

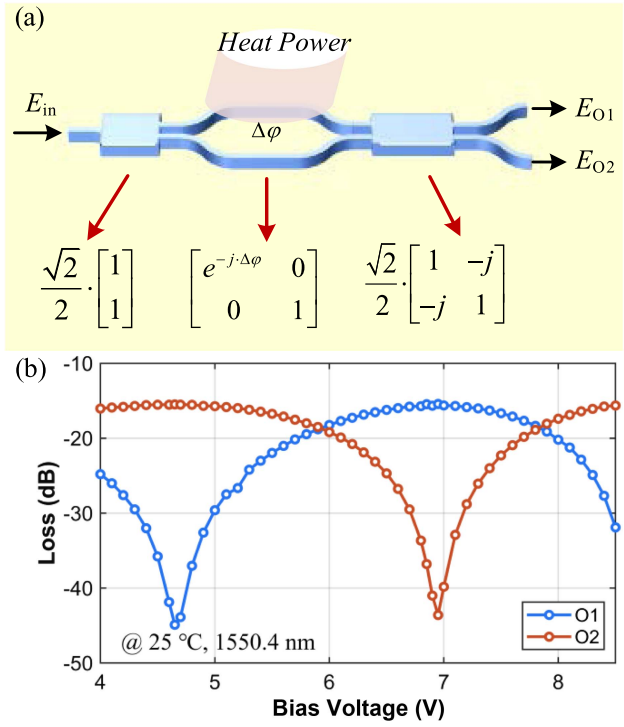

Fig. 11. (a) 3D diagram of MZI-based tunable coupler. (b) Output powers verus bias voltage of the tunable coupler.

output powers at both output ports can be adjusted by inducing a phase difference between the optical arms via the TOPSs, and the transfer matrix of this device can be analytically derived as shown in Fig. 11(a).

By applying varied bias voltages to the metal pads connected to the TOPS heaters, we characterized the output power versus bias voltage relationship as depicted in Fig. 11(b). This characterization provides a definitive reference for precise power-splitting ratio adjustments. Since both ring cavities and the tunable coupler are thermally tuned simultaneously, their respective microheaters are placed far apart to minimize thermal crosstalk. To further enhance thermal isolation, a deep trench process could be implemented between heaters, which would improve both thermal isolation and tuning efficiency.

APPENDIX B: GUARD BAND OPTIMIZATION

As detailed in the main text, the value of the signal guard band has been optimized via normalized generalized mutual information (NGMI) performance of the integrated CESC receiver. Notably, a critical trade-off exists between electrical spectral efficiency (ESE) and filtered carrier purity: narrower guard bands enhance ESE but increase residual signal components, degrading carrier purity. This introduces non-negligible SSBI penalties as more signal power leaks through the filter. Conversely, wider guard bands ensure carrier purity and receiver performance at the expense of ESE.

Also, the received-signal optical spectra with a 3-GHz guard band before and after filtering have been shown in the main text. Therefore, we supplement the before and after-filtering signal optical spectra with varied guard bands (0.5, 1, 2, 4, 5, and 6 GHz) to characterize the powers of residual signal components with varied guard bands and the suppression capability of the narrowband CROW filter, as presented in Fig. 12. Thereby, the narrowband filter can be further optimized based on these results in future work. When the signal guard band is ≥2 GHz, the signal components have been well suppressed, as depicted in Figs. 12(e) and 12(f). Furthermore, Figs. 12(g) and 12(h) demonstrate that the residual signal terms become negligible while the signal guard band is extended beyond 4 GHz.

Notably, although a wider guard band enhances the purity of the extracted carrier and better suppresses SSBI, excessively wide guard bands would waste large amounts of low-frequency spectral resources, introducing some transmission impairments such as exceeding the electro-optic bandwidth of active devices and incurring more severe high-frequency attenuation. These factors can degrade overall system performance and ESE. Therefore, the guard band should be optimized holistically based on overall system performance, rather than considering carrier purity alone.

Funding. National Natural Science Foundation of China (62471404, 62341508); Key Project of Westlake Institute for Optoelectronics (2023GD003).

Disclosures. The authors declare no conflicts of interest.

Data Availability. Data underlying the results presented in this paper are not publicly available at this time but may be obtained from the authors upon reasonable request.

REFERENCES

1. Q. Cheng, M. Bahadori, M. Glick, *et al.*, "Recent advances in optical technologies for data centers: a review," Optica **5**, 1354–1370 (2018).

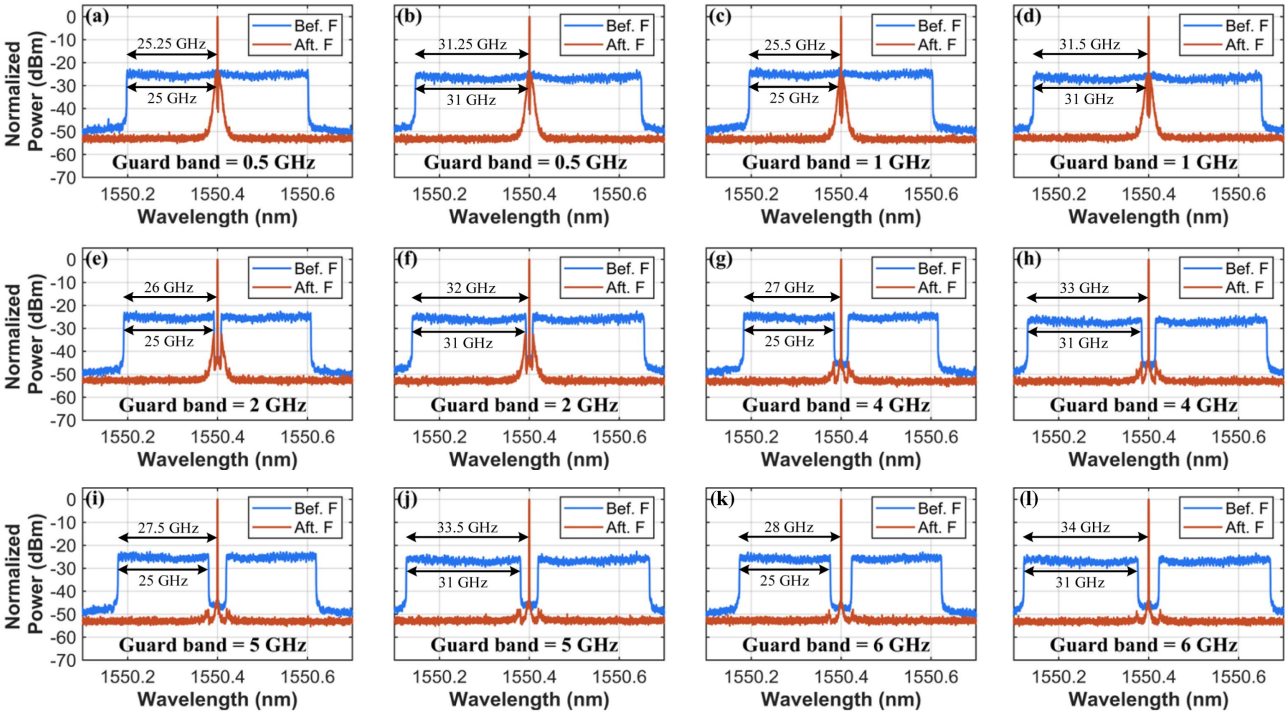

Fig. 12. (a)–(l) Optical spectra of 50- and 62-Gbaud signals before and after filtering with varied signal guard bands.

2. X. Zhou, D. Yi, D. W. U. Chan, *et al.*, "Silicon photonics for high-speed communications and photonic signal processing," npj Nanophotonics **1**, 27 (2024).
3. K. Zhong, X. Zhou, J. Huo, *et al.*, "Digital signal processing for short-reach optical communications: a review of current technologies and future trends," J. Lightwave Technol. **36**, 377–400 (2018).
4. A. Rizzo, A. Novick, V. Gopal, *et al.*, "Massively scalable Kerr comb-driven silicon photonic link," Nat. Photon. **17**, 781–790 (2023).
5. D. Shi, P. Yuan, H. Zhu, *et al.*, "Energy consumption comparison of IM/DD, coherent, and Kerr-comb-WDM architectures for intra-datacenter applications," in *Proceedings of the 50th European Conference on Optical Communication (ECOC)* (2024), pp. 1106–1109.
6. D. Che and X. Chen, "Modulation format and digital signal processing for IM-DD optics at post-200G era," J. Lightwave Technol. **42**, 588–605 (2024).
7. X. Pang, O. Ozolins, R. Lin, *et al.*, "200 Gbps/lane IM/DD technologies for short reach optical interconnects," J. Lightwave Technol. **38**, 492–503 (2020).
8. X. Zhou, R. Urata, and H. Liu, "Beyond 1 Tb/s intra-data center interconnect technology: IM-DD or coherent?" J. Lightwave Technol. **38**, 475–484 (2019).
9. E. Ip, A. P. T. Lau, D. J. Barros, *et al.*, "Coherent detection in optical fiber systems," Opt. Express **16**, 753–791 (2008).
10. J. Zhang, Z. Dong, J. Yu, *et al.*, "Simplified coherent receiver with heterodyne detection of eight-channel 50 Gb/s PDM-QPSK WDM signal after 1040 km SMF-28 transmission," Opt. Lett. **37**, 4050–4052 (2012).
11. W. Shieh, C. Sun, and H. Ji, "Carrier-assisted differential detection," Light: Sci. Appl. **9**, 18 (2020).
12. H. Ji, S. Dong, Z. Xu, *et al.*, "Carrier assisted differential detection with generalized and simplified receiver structure," J. Lightwave Technol. **39**, 7159–7167 (2021).
13. D. Che, A. Li, X. Chen, *et al.*, "Stokes vector direct detection for linear complex optical channels," J. Lightwave Technol. **33**, 678–684 (2015).
14. A. Mecozzi, C. Antonelli, and M. Shtaif, "Kramers–Kronig coherent receiver," Optica **3**, 1220–1227 (2016).
15. Y. Shi, Y. Zhang, Y. Wan, *et al.*, "Silicon photonics for high-capacity data communications," Photon. Res. **10**, A106–A134 (2022).
16. N. Margalit, C. Xiang, S. M. Bowers, *et al.*, "Perspective on the future of silicon photonics and electronics," Appl. Phys. Lett. **118**, 220501 (2021).
17. S. Bernabé, Q. Wilmart, K. Hasharoni, *et al.*, "Silicon photonics for terabit/s communication in data centers and exascale computers," Solid-State Electron. **179**, 107928 (2021).
18. D. Thomson, A. Zilkie, J. E. Bowers, *et al.*, "Roadmap on silicon photonics," J. Opt. **18**, 073003 (2016).
19. J. Li, Z. Wang, H. Ji, *et al.*, "Silicon photonic carrier-assisted differential detection receiver with high electrical spectral efficiency for short-reach interconnects," J. Lightwave Technol. **41**, 919–925 (2023).
20. P. Dong, X. Chen, K. Kim, *et al.*, "128-Gb/s 100-km transmission with direct detection using silicon photonic Stokes vector receiver and I/Q modulator," Opt. Express **24**, 14208–14214 (2016).
21. H. Zhu, Y. Fang, J. Wu, *et al.*, "Narrow-bandwidth silicon photonic CROW filter for carrier-extracted self-coherent (CESC) detection," Opt. Lett. **49**, 5151–5154 (2024).
22. J. Li, Z. Wang, X. Li, *et al.*, "Four-dimensional silicon photonic dual-polarization direct detection receiver," J. Lightwave Technol. **42**, 4031–4037 (2024).
23. T. Gui, X. Wang, M. Tang, *et al.*, "Real-time demonstration of homodyne coherent bidirectional transmission for next-generation data center interconnects," J. Lightwave Technol. **39**, 1231–1238 (2021).
24. H. Zhu, Y. Fang, Y. Xie, *et al.*, "Ultra-narrow-bandwidth silicon photonic tunable second-order CROW filter with low insertion loss for carrier-extracted self-coherent (CESC) detection," in *Proceedings of Optical Fiber Communications Conference and Exhibition (OFC)* (2025), pp. 1–3.
25. W. Bogaerts, P. D. Heyn, T. V. Vaerenbergh, *et al.*, "Silicon microring resonators," Laser Photonics Rev. **6**, 47–73 (2012).
26. L. Zhang, H. Zhao, H. Wang, *et al.*, "Cascading second-order microring resonators for a box-like filter response," J. Lightwave Technol. **35**, 5347–5360 (2017).
27. H.-C. Liu and A. Yariv, "Synthesis of high-order bandpass filters based on coupled-resonator optical waveguides (CROWs)," Opt. Express **19**, 17653–17668 (2011).
28. D. A. Fishman and J. A. Nagel, "Degradations due to stimulated Brillouin scattering in multigigabit intensity-modulated fiber-optic systems," J. Lightwave Technol. **11**, 1721–1728 (1993).
29. I. Sackey, T. Richter, M. Nölle, *et al.*, "Qualitative comparison of Kerr nonlinearity mitigation schemes in a dispersion-managed link for 4×28-GBd 16-QAM signals," J. Lightwave Technol. **33**, 4815–4825 (2015).
30. H. Ji, Z. Wang, X. Li, *et al.*, "Photonic integrated self-coherent homodyne receiver without optical polarization control for polarization-multiplexing short-reach optical interconnects," J. Lightwave Technol. **41**, 911–918 (2022).
31. D. Che and W. Shieh, "Entropy-loading: multi-carrier constellation-shaping for colored-SNR optical channels," in *Proceedings of Optical Fiber Communication Conference and Exhibition (OFC)* (2017), pp. 1–3.
32. D. Shi, W. Lu, Y. Fang, *et al.*, "Entropy-loading enhanced 300 GHz DP-IM/DD photonic-assisted THz wireless interconnect," J. Lightwave Technol. **43**, 8729–8736 (2025).
33. F. P. Payne and J. P. R. Lacey, "A theoretical analysis of scattering loss from planar optical waveguides," Opt. Quant. Electron. **26**, 977–986 (1994).
34. L. Zhang, L. Jie, M. Zhang, *et al.*, "Ultrahigh-*Q* silicon racetrack resonators," Photon. Res. **8**, 684–689 (2020).
35. C. K. Madsen, P. Oswald, M. Cappuzzo, *et al.*, "Reset-free integrated polarization controller using phase shifters," J. Sel. Top. Quant. Electron. **11**, 431–438 (2005).
36. W. Liu, J. Liao, H. Cai, *et al.*, "High-speed silicon integrated polarization stabilizer assisted by a polarimeter," J. Lightwave Technol. **40**, 3794–3801 (2022).
37. S. Chen, Y. Shi, S. He, *et al.*, "Low-loss and broadband 2×2 silicon thermo-optic Mach–Zehnder switch with bent directional couplers," Opt. Lett. **41**, 836–839 (2016).
38. S. Hong, J. Wu, Y. Xie, *et al.*, "Versatile parallel signal processing with a scalable silicon photonic chip," Nat. Commun. **16**, 288 (2025).